Placing Limits on Light Axions with EHT Polarimetry via Closure Traces

by

Zhiren Wang

A thesis
presented to the University of Waterloo
in fulfillment of the
thesis requirement for the degree of
Master of Science
in
Physics

Waterloo, Ontario, Canada, 2023

Author's Declaration

I hereby declare that I am the sole author of this thesis. This is a true copy of the thesis, including any required final revisions, as accepted by my examiners.

I understand that my thesis may be made electronically available to the public.

Abstract

Black holes can amplify incoming bosonic waves via rotational superradiance, inducing bound states of ultralight bosons around them. This phenomenon has the potential to confine the parameter spaces of new bosons. Axions, and axion-like particles (ALPs) are candidates beyond-standard-model particles that can form such clouds around supermassive black holes (SMBHs) and impact the polarization signal in a similar fashion to Faraday rotation via axion-photon coupling. Prior research has used data from the Event Horizon Telescope (EHT) M87 2017 observations to limit the dimensionless axion-photon coupling to previously unexplored regions. With the novel calibration-insensitive quantities: closure traces and conjugate closure trace products, it is possible to constrain the existence of axion clouds while avoiding the most dominant sources of systematic uncertainties, e.g., station gains and polarization leakages. I utilize a simple geometric model for the polarization map of M87* to fit the model parameters with both simulated and real datasets to verify the applicability of this method and reach a comparable level of constraint in the accuracy with which an axion cloud may be excluded in M87. Such approach is feasible with application to future M87* and Sgr A* observations by EHT and next-generation EHT (ngEHT) and may provide stronger constraints on axions and ALPs.

Acknowledgements

First of all, I am extremly grateful to my supervisor, Dr. Avery Broderick for his clear guidance, invaluable advice, continuous support, and patience during my master study. His immense knowledge and plentiful experience have encouraged me in all the time. I would also like to thank Dr. Asimina Arvanitaki for her overarching explantions of the research topic and Dr. Yifan Chen for his explanations regarding the research details. Finally, I would like to thank all the members in our group. Their kind help and support have made my academic and daily life enjoyable.

Dedication

This is for my parents, who have both physcially and mentally supported me throughout these years no matter what happened.

Table of Contents

List of Figures

List of Tables

Chapter 1

Introduction

Active Galactic Nuclei (AGN), found at the centers of galaxies, are a type of extremely luminous and persistent astronomical object that can be easily distinguished from the rest of the host galaxies. These objects are theorized to be powered by the accretion of gas onto supermassive black holes (SMBHs) with masses ranging from millions to billions solar masses [Alston et al., 2022]. Gas in proximity to the central engine is ionized, along with strong, turbulent electromagnetic fields, and relativistically accelerated particles. Therefore, AGNs exhibit broad-band spectral energy distributions (SEDs), spanning from radio waves to gamma rays. Radio waves from AGNs encode essential information about the magnetic fields and relativistic flows near the central SMBH. Furthermore, the Event Horizon Telescope Collaboration (EHTC) has recently published images that resolved the horizon-scale structures surrounding M87*, a recent major achievement of radio observations [M87* Paper I]. In this thesis, I present a interdisciplinary study between radio astronomy and particle physics by relating radio observation data and parameters of a hypothetical particle.

The structure of this work is as follows. In Chapter 1, I provide an overview on AGN observations and one application. In Chapter 2, I introduce my model of electric vector position angle (EVPA) variations, explore and discuss its feasibility. In Chapter 3, I present the Monte Carlo Markov Chain (MCMC) fits for the model and its implications. Finally, in Chapter 4 I present the conclusions.

1.1 Multiwavelength Observations of AGNs

Being the most luminous type of astronomical object in electromagnetic radiation in the universe, AGN are observed and studied across the entire electromagnetic spectrum. For example, in the radio regime, AGN are identified as extragalactic sources of synchrotron emission, which arises from the interaction of relativistic electrons with magnetic fields. The radio emission from AGN is often highly variable and can be used to study the properties of the relativistic outflows that are launched from the vicinity of the SMBH [Boccardi et al., 2017]. Furthermore, radio observations of AGNs are constantly pushing the limit of the resolution of images of those cosmic giants, revealing their complicated magnetic structures. In fact, highly resolved images of SMBHs by poking deeply into AGNs through modern intereferometry techniques would be the subject of this thesis.

In addition to radio observations, multiwavelength studies of AGNs also play an important role in understanding them. In the optical and ultraviolet (UV) regimes, AGN are identified as point-like sources that exhibit strong and broad emission lines in their spectra [Peterson, 1997]. The broad emission lines arise from ionized gas that is located in a region known as the broad-line region (BLR), at distances of a few light-days to a few light-weeks from the SMBH [Czerny and Hryniewicz, 2011]. The narrow emission lines, with widths of only a few hundred kilometers per second, are produced in gas clouds located further out in the galaxy, at distances of tens to hundreds of parsecs [Heckman et al., 1981]. The broadening can provide reliable estimate of the mass of central SMBHs [Gaskell, 2009]. The UV and optical emission from AGN is highly variable on timescales ranging from minutes to years, and can be used to study the physical properties of the accretion disk surrounding the SMBH. In the X-ray regime, AGN are highly luminous and often obscured, which indicates the presence of a thick torus of gas and dust that surrounds the SMBH. X-ray observations can penetrate this obscuring material and reveal the hard X-ray emission that is produced in the corona of the accretion disk [Shields, 1999]. X-ray observations of AGN have revealed the presence of outflows that are launched from the vicinity of the SMBH, which can carry significant amounts of mass and energy away from the central regions of the galaxy [Barcons, 2001]. Observations in other band such as infrared (IR) and γ ray exist as well[Padovani, 2017].

1.2 Polarization Analysis with Very Long Baseline Interferometry

Among the multiple pathways in the radio study of AGN, polarization observation of those targets and their central engines plays a crucial role in unveiling the inner structures, especially the intrinsic magnetic fields of these cosmic giants [Johnson et al., 2015,M87* Paper VII]. Fortunately, the advent of very long baseline interferometry (VLBI) has enabled us to overcome the challenge posed by their extremely small angular sizes, allowing for detailed analyses of their vicinity [Thompson et al., 2017]. Polarization signals from those massive giants encode essential information about the dynamics and magnetic structures in the surrounding environments. In 2021, the Event Horizon Telescope Collaboration presented the first horizon-resolving polarimetric images of M87* shadow [M87* Paper VII], enabling unprecedented detailed analysis of its physics.

1.2.1 The Event Horizon Telescope

The EHT is a global VLBI experiment containing multiple ground-based radio telescopes, which emulates a virtual telescope with effective size close to the diameter of the Earth. Each telescope pair introduces a baseline that scans through the sky as the Earth rotates. Radio waves from the source received at each site are sampled and recorded with a precise local atomic clock, and correlated by searching the delay space for the actual relative times. Recorded data is then transported to a central location after observations and cross-correlated with respect to each telescope pair [M87* Paper I]. During the EHT 2017 Campaign, a total of eight telescopes were involved in the observations, including the Atacama Large Millimeter/submillimeter Array (ALMA), the Atacama Pathfinder Experiment telescope (APEX) in Chile, the James Clerk Maxwell Telescope (JCMT) and the Submillimeter Array (SMA) in Hawai'i, the Large Millimeter Telescope Alfonso Serrano (LMT) in Mexico, the Submillimeter Telescope Observatory (SMT) in Arizona, the IRAM 30 m telescope on Pico Veleta (PV) in Spain, and the South Pole Telescope (SPT) in Antarctica. Figure 1.1 shows the locations of these ground-based telescopes. Additional sites such as the Greenland Telescope (GLT), the Kitt Peak 12m Radio Telescope (KP) and the Northern Extended Millimeter Array (NOEMA) were involved in later campaigns. Operations at a wavelength of 1.3mm in full polarimetric mode and at multiple sites in different continents ensured an unprecedented level of sensitivity and sufficiently long baseline lengths for horizon-scale imaging. More details are discussed in M87* Paper II.

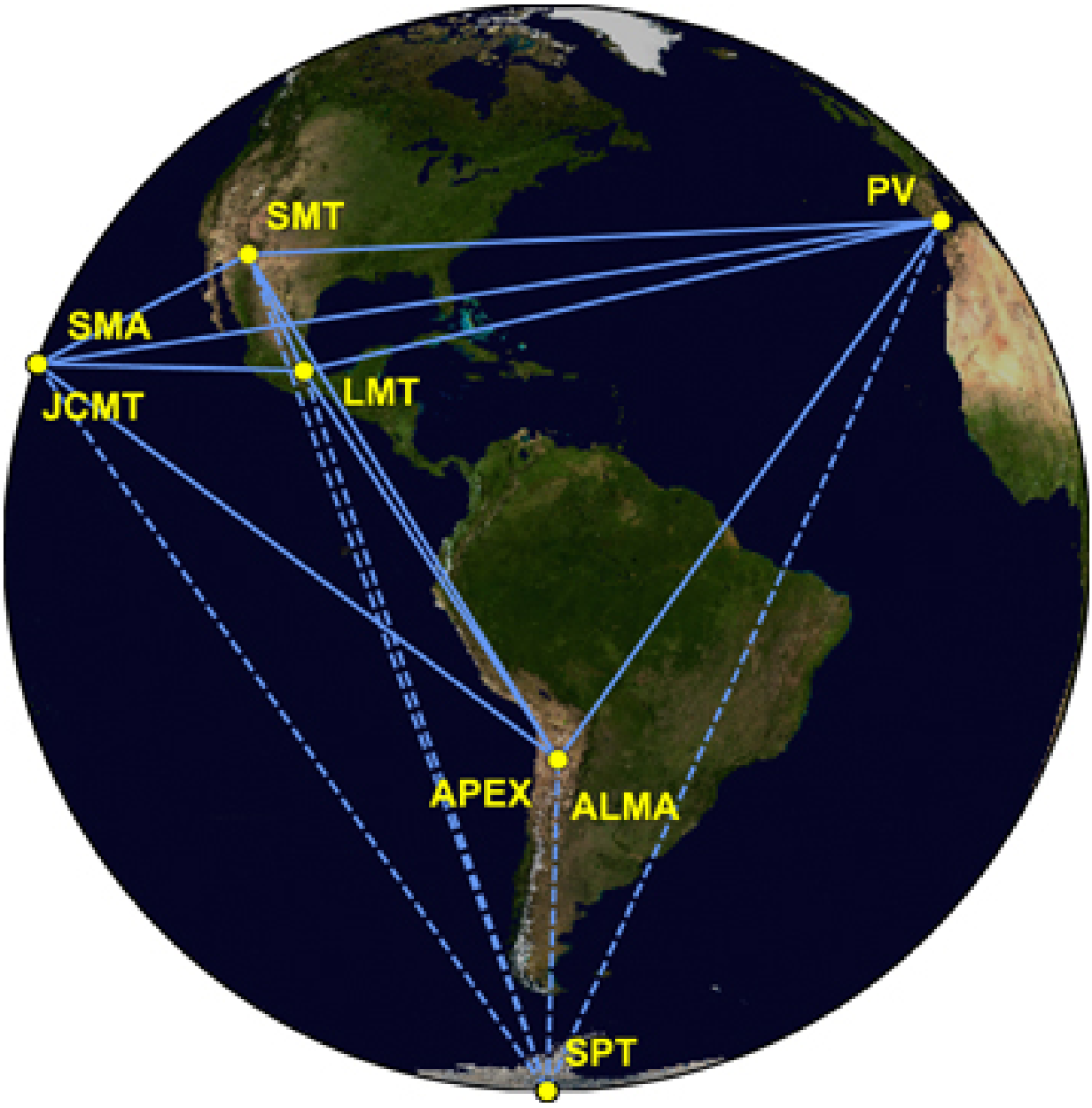

Figure 1.1: Eight stations involved in the EHT 2017 observations. Seven of them connected by solid baselines were used for M87*, while the dashed baselines and SPT were used for the calibrator 3C279 [M87* Paper I].

1.2.2 Polarimetric VLBI Concepts

Some basic concepts related to radio interferometry and polarimetry are introduced below [Thompson et al. 2017, M87* Paper I]. The polarization state of electromagnetic radiation is described by four Stokes parameters $\mathcal{I}$ (total intensity), $\mathcal{Q}$ (linear polarization component in vertical and horizontal directions), $\mathcal{U}$ (linear polarization component at 45° and -45° position angle), and $\mathcal{V}$ (circular polarization component). The complex linear polarization $\mathcal{P}$ can be defined as

$$\mathcal{P} = \mathcal{Q} + i\mathcal{U} = \mathcal{I}|m|e^{2i\chi} \tag{1.1}$$

where $m = (\mathcal{Q}+i\mathcal{U})/\mathcal{I}$ represents the (complex) fractional polarization and $\chi = 0.5\arg(\mathcal{P})$ is the electric vector position angle (EVPA). It is the modelling of variations of the EVPA that will be the primary focus of this thesis. It also follows that the degree of linear (m_l), circular (m_c) and total (m_t) polarization can be expressed as

$$m_l = \frac{\sqrt{\mathcal{Q}^2 + \mathcal{U}^2}}{\mathcal{I}} \tag{1.2}$$

$$m_c = \frac{\mathcal{V}}{\mathcal{I}} \tag{1.3}$$

$$m_t = \frac{\sqrt{\mathcal{Q}^2 + \mathcal{U}^2 + \mathcal{V}^2}}{\mathcal{I}} \tag{1.4}$$

The primary data products in EHT are in fact the complex correlation products between the electric fields incident at each telescope in the array (see, e.g., Broderick and Pesce, 2020). In a circular basis with indices ij referring to the two stations defining a particular baseline, they are

$$RR_{ij} = \langle E_{R,i} E^*_{R,j} \rangle \tag{1.5}$$

$$LL_{ij} = \langle E_{L,i} E^*_{L,j} \rangle \tag{1.6}$$

$$RL_{ij} = \langle E_{R,i} E^*_{L,j} \rangle \tag{1.7}$$

$$LR_{ij} = \langle E_{L,i} E^*_{R,j} \rangle \tag{1.8}$$

where E is the electric field, R and L indicate right-hand and left-hand circular polarization respectively, and an asterisk denotes complex conjugation. These correlations reveal the Fourier transform of the target emission structure through the van Cittert-Zernike theorem [Thompson et al., 2017]. We can then relate the correlation products and the Fourier transform of the Stokes parameters (Stokes visibility) in the following way:

$$\bar{\boldsymbol{V}}_{ij} = \begin{pmatrix} RR_{ij} & LL_{ij} \\ RL_{ij} & LR_{ij} \end{pmatrix} = \begin{pmatrix} \tilde{\mathcal{I}}_{ij} + \tilde{\mathcal{V}}_{ij} & \tilde{\mathcal{Q}}_{ij} + i\tilde{\mathcal{U}}_{ij} \\ \tilde{\mathcal{Q}}_{ij} - i\tilde{\mathcal{U}}_{ij} & \tilde{\mathcal{I}}_{ij} - \tilde{\mathcal{V}}_{ij} \end{pmatrix} \tag{1.9}$$

One can invert Equation 1.9 and inverse Fourier transform the Stokes visibility components to reconstruct the actual polarimetric images.

Despite its many advantages, polarized radio interferometry, which is used to generate the polarimetric images of M87*, suffers from multiple systematic uncertainties, including station gains that modulate both the amplitude and the phase of the observed signal, and polarimetric leakages from one channel to another, e.g., from right-hand circular polariztion to left-hand circular polarization [M87* Paper III]. The former one can be circumvented by "closure" quantities (closure phase and closure amplitude) on multiple sites that are immune to station-based effect because station-based gain errors are cancelled out [Jennison, 1958, Twiss et al., 1960, Readhead et al., 1980], while the latter one is calibrated with suboptimal assumptions [M87* Paper VII]. Luckily, Broderick and Pesce [2020] introduced a novel calibration-insensitive closure quantity: closure trace (CT), defined on station quadrangles, that is insensitive to station gains and polarimetric leakages (D-terms) and comprises all calibration-independent information in the visibility data; and a subsequent quantity, the conjugate closure trace product (CCTP), that can serve as a robust indicator of polarization sources. Additional details are explained in Chapter 2.

1.3 Studying Hypothetical Particles with AGN

Besides the study of magnetic structures [M87* Paper VIII], the acceleration of the bulk flow, and the relativistic heating of jet constituents [Hada et al., 2018], SMBHs offer a unique opportunity to probe beyond-standard model (BSM) physics and place constraints on speculative particles [Arvanitaki and Dubovsky, 2011]. Examples include QCD (quantum chromodynamics) axions, which have been proposed as a solution to the strong CP (charge-parity symmetry) problem, and axion-like particles (ALPs).

CP symmetry suggests that the laws of physics should behave the same way if you replace particles with antiparticles (charge) and mirror the system (parity). The symmetry is broken in the Standard Model through weak interactions, and is expected to be broken in strong intereactions as well, according to the current mathematical formulation of QCD. Specifically, there is a "theta term" that violates CP symmetry. If this term is large, it would lead to observable effects that are still not yet seen in experiments [Hook, 2018]. Then there is the strong CP problem: Experiments have shown that the strong CP-violating effects are much smaller than what would be expected if the theta term were of typical size.

The introduction of axions, as proposed by Peccei and Quinn, provides a mechanism that naturally explains the observed CP conservation by dynamically adjust the value of

the theta term in the strong interaction [Peccei and Quinn, 1977]. In addition, axions and ALPs have also emerged as compelling candidates for dark matter [Preskill et al., 1983]. The observed gravitational effects in galaxies and cosmological structures indicate the presence of significant amounts of invisible mass, referred to as dark matter. Axions and ALPs, due to their weak interactions with ordinary matter and their potential to form cold, non-relativistic particles, could constitute the missing dark matter component and help resolve the long-standing mystery of its nature. Extensive experimental efforts are underway to detect and study axions and ALPs, employing various techniques such as resonant cavities (axion haloscope), laser-based experiments with equipment in laboratories, and observations of axion-photon converion in astrophysical magnetic fields with telescopes [Adams et al., 2022]. The third approach is widely utilized in modern astrophysics [Millar et al., 2021, Mirizzi et al., 2008]. For example, by carefully studying the polarization properties of light from distant sources or the polarization of the cosmic microwave background (CMB) radiation, one can search for distinct signatures that indicate the presence of axions and provide valuable insights into their properties and existence. In particular, the polarization of light around SMBHs provides a unique way of studying axions and ALPs.

To begin with, axions would accumulate around black holes via black hole superradiance, under which traveling light bosons form bound states around SMBHs and grow exponentially as long as superradiance condition, $\omega < m\Omega_H$, is satisfied. ω is the frequency of the incoming wave, Ω_H is the angular frequency of the black hole and m is the azimuthal quantum number (see Figure 1.2). In addition, the most significant superradiant rate occurs when $m = 1$, the lowest possible energy state that satisfies the condition [Dolan, 2007]. The superradiant rate is maximized when the axion's reduced Compton wavelength λ_c is comparable to the black hole size [Arvanitaki et al., 2015]. This process is maximized when In the presence of a background axion field, the modification of a photon's equation of motion due to the axion-photon interaction will introduce a periodic oscillation to the EVPAs of linearly polarized photons [Carroll et al., 1990, Carroll and Field, 1991, Harari and Sikivie, 1992]. Theoretically, modelling the variations of EVPAs around the shadow of an SMBH should indicate novel constraints on light axions aside from previous results[1].

An experiment was then proposed when Chen et al. [2020] addressed that this axion-induced birefringence effect can cause the EVPAs on the photon ring of an SMBH to vary with time and position. In the condition of photon propagating in a background axion field, axion-photon interaction modifies the Lagrangian as

$$\mathcal{L} = -\frac{1}{4}F_{\mu\nu}F^{\mu\nu} - \frac{1}{2}g_{a\gamma}aF_{\mu\nu}\tilde{F}^{\mu\nu} + \frac{1}{2}\nabla^{\mu}a\nabla_{\mu}a - V(a), \tag{1.10}$$

[1]For an extensive compilation of existing experimental axion constraints from the literature, ecompassing a broad range of potential masses, see cajohare.github.io/AxionLimits/docs/ap.html [O'Hare, 2020].

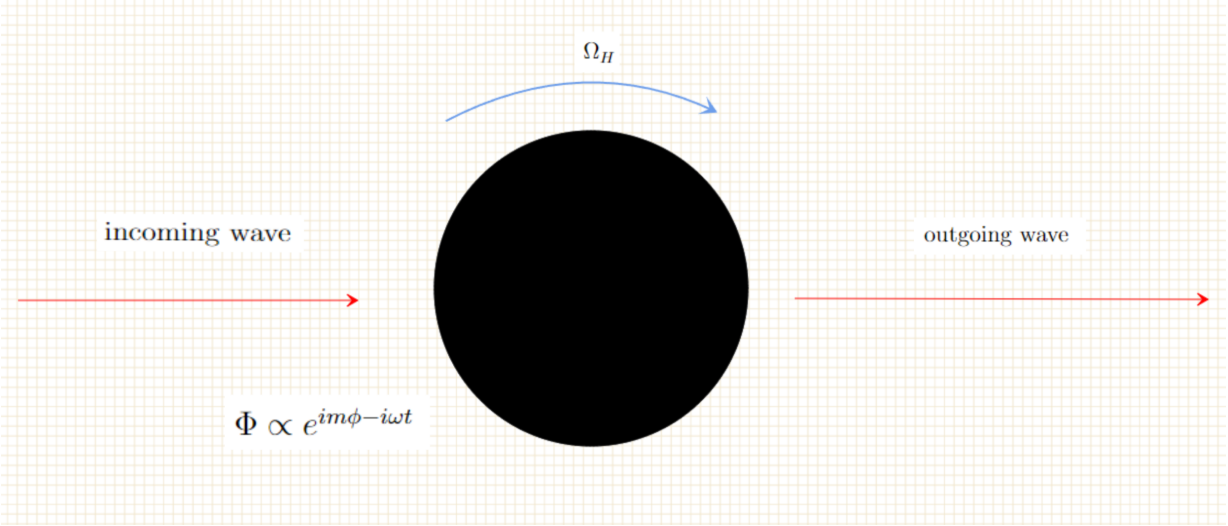

Figure 1.2: A schematic for black hole superradiance. Note that Φ describes the form of the wave function.

in which $g_{a\gamma}$ is the axion-photon coupling constant, $F_{\mu\nu}$ is the electromagnetic tensor and $\tilde{F}^{\mu\nu}$ is its dual tensor. A naive deduction would be that this axion-induced effect would function very similarly to the normal Faraday effect. Successive derivations with the assumption that the photon frequency is much larger than axion's reduced Compton wavelength λ_c reached a simple expression for the EVPA rotation of a linearly polarized photon:

$$\Delta\theta = g_{a\gamma}[a(t_{\rm obs}, \boldsymbol{x}_{\rm obs}) - a(t_{\rm emit}, \boldsymbol{x}_{\rm emit})] \tag{1.11}$$

The rotation only depends on the difference between the emitting and observing axion field values. With further appropriate assumptions and simplifications that describe the EVPA variation in Boyer-Lindquist coordinates of the black hole, the final form can be parametrized like

$$\Delta\theta(t, \phi) = \mathcal{A}(\phi)\cos[\omega t + \phi + \beta(\phi)], \tag{1.12}$$

in which a polar coordinate (r, ϕ) centered at the black hole shadow is used. For a detailed derivation of the previous equations, see Chen et al. [2022a]. Recently, a practical attempt by the same group [Chen et al., 2022b] utilize the polarimetric information of M87* [M87* Paper VII] to reach a previously unexplored parameter space of light axions. Specifically, they implement constraints on the joint distribution of the axion mass m_a and the dimensionless axion-photon coupling constant $c_{a\gamma} \equiv 2\pi g_{a\gamma} f_a$. However, one caveat is that the parametrized form of EVPA variation relies on the assumption of a saturated ax-

ion cloud. While it is impossible to know if the axion cloud is saturated given the unknown recent astrophysical history of M87, I adopt this assumption henceforth (see Chen et al. [2022a] for a full discussion of this issue).

Therefore, based on the information of axion-photon coupling and CT analysis, I present a new method to constrain light axions and demonstrate that it can reach a roughly similar level of constraint as Chen et al. [2022b]. This method, being insensitive to a much larger class of errors than ameliorated by gains and D-terms, circumvents the time-consuming direct calibration process to the final polarized images of M87* and is complete in retrieving polarimetric information. This novel method can be further applied to future EHT and next-generation EHT (ngEHT) observations [Johnson et al., 2023], for which more quadrangles will be available, to reach stronger constraints on axions, ALPs and other ultralight bosons.

Chapter 2

A Simple Geometric Model for the Linear Polarization Maps of M87*

The most striking feature of the EHT images of M87* (Figure 2.1) is the clear presence of a ring, presumably encircling the black hole shadow. Upon this ring lies a "twisty" linear polarization pattern with the EVPA exhibiting a nearly linear dependence on azimuth. Given these gross features, I generate a simple geometric model for the polarized images of M87* with which to explore the constraints made possible using the measured CCTPs.

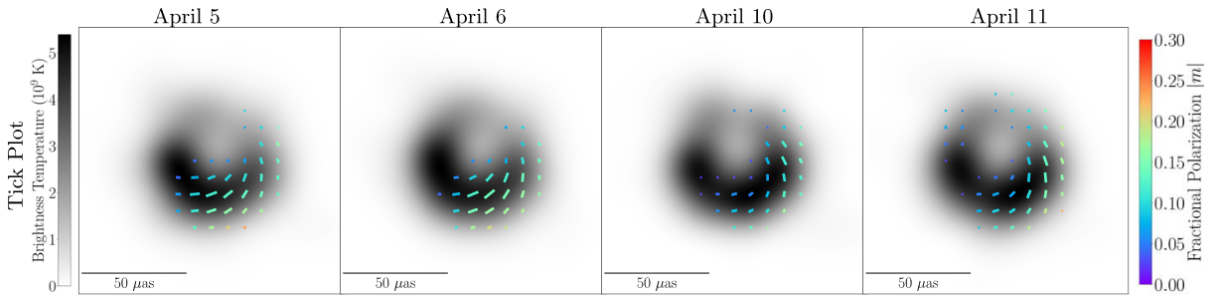

Figure 2.1: Fiducial average polarimetric images of M87* from EHT 2017 Campaign [M87* Paper VII].

2.1 Image Domain Model

Besides the outstanding feature of an annulus in the EHT images of M87*, I clearly notice the position angle of the maximum Stokes $\mathcal{I}$ map lies in the southern direction, the position angle of the maximum linear polarization lies in the SW direction and the EVPA position angle around the shadow appears to deviate from an overall radial EVPA pattern (Figure 2.1). Based on this information and putting time-dependent EVPA variations aside, I begin by creating movie objects to model the flux and the polarization map, that can be processed by `eht-imaging` [Chael et al., 2018]. The parameters include the diameter d of the annular emission region in μas, annulus width w, linear polarization fraction m, the number of periods $n_{\rm cyc}$ per 24 h, the position angle $\Phi_{\rm I}$ of the maximum brightness in Stokes $\mathcal{I}$ map and the position angle $\Phi_{\rm pol}$ of the maximum polarized flux, where the latter two angles start from 0 in the south direction on the image and increase clockwise, i.e.,

$$\mathcal{I}(r,\phi;\mathcal{I}_0,d,w,\Phi_{\rm I}) = \mathcal{I}_0 \begin{cases} \cos^2\left[(\phi+\Phi_{\rm I})/2\right] & \text{if } d-w<r<d \\ 0 & \text{otherwise,} \end{cases} \tag{2.1}$$

and

$$|\mathcal{P}|(r,\phi;\mathcal{I}_0,d,w,\Phi_{\rm pol}) = m\mathcal{I}_0 \begin{cases} \cos^2\left[(\phi+\Phi_{\rm pol})/2\right] & \text{if } d-w<r<d \\ 0 & \text{otherwise.} \end{cases} \tag{2.2}$$

Given an EVPA, $\theta(t,\phi)$, I can then construct the remaining Stokes parameters via

$$\begin{aligned} \mathcal{Q}(r,\phi;\mathcal{I}_0,d,w,\Phi_{\rm pol},\theta) &= |\mathcal{P}|(r,\phi;\mathcal{I}_0,d,w,\Phi_{\rm pol})\cos\left[2\theta(t,\phi)+2\phi\right] \\ \mathcal{U}(r,\phi;\mathcal{I}_0,d,w,\Phi_{\rm pol},\theta) &= |\mathcal{P}|(r,\phi;\mathcal{I}_0,d,w,\Phi_{\rm pol})\sin\left[2\theta(t,\phi)+2\phi\right]. \end{aligned} \tag{2.3}$$

After convolving the polarimetric images by a Gaussian filter, I can then generate movies that reflect the time evolution of EVPAs that results from axion-photon coupling. Combining the most prominent features of the polarized images of M87* and the parametrization of EVPA variation by Chen et al. [2022b], I construct a simple geometric model of the EVPA oscillation by introducing an additional time-dependent position angle θ on top of a fundamental time-independent radial EVPA pattern (Figure 2.2) around the shadow.

$$\theta(t,\phi) = \theta_0 + \theta_1\cos\left[\omega(t - r_{\rm ring}\sin 17^\circ\cos\phi) + \phi + \delta\right] \tag{2.4}$$

In this model, θ_1 is the oscillation amplitude and is proportional to $c_{a\gamma}$ and ω is the axion angular frequency proportional to m_a. The rest of the parameters are defined as follows: $r_{\rm ring} = \sqrt{27}r_{\rm g}$ is the radius of the shadow (assuming a=0) of M87*, θ_0 is the initial value of θ, ϕ is the azimuthal angle on the annulus and δ describes an arbitrary initial phase. θ_1 is

independent of the azimuthal angle because the azimuthal variation is rather marginal, as seen in Chen et al. [2022b]. Figure 2.2 shown below is the fundamental radial EVPA plot I start from, while in Figure 2.3 I add θ and clip a total of eight frames from the EVPA movie on parameters of 2017 April 11 to fully cover its evolution. This simple geometric model captures the characteristics of time-dependent EVPA variation induced by axion-photon coupling appearing as propagating waves around the shadow.

Chen et al. [2022b] extended the "forbidden" region of axions on the $c_{a\gamma}$-m_a parameter space by directly fitting the differential EVPA on the polarimetric images across 2017 April 5, 6, 10, 11, highlighting the possibility of exploring new physics with the unprecedented EHT images on SMBHs (although assuming the existence of a saturated, superradiantly generated axion cloud around M87*). However, it is important to note that this approach neglect the systematic uncertainties within the EVPA, like station gains and D-terms, which will be discussed below, associated with calibrations to the final polarimetric images. This new method, on the other hand, takes advantage of novel calibration-insensitive quantities for radio astronomy, to "observe" the time-dependent movies generated by this model, and reach an approximately comparable level of constraints on light axions, without the need for full polarimetric image reconstruction, with the attendant systematic uncertainties.

2.2 Constructing EHT Observables

The primary EHT data products are visibilities, corresponding to the Fourier transform of the Stokes $\mathcal{I}$, $\mathcal{Q}$, $\mathcal{U}$, and $\mathcal{V}$ brightness maps. I obtain these using the `eht-imaging` package via the *observe* function, generating visibilities in the more common circular basis, RR, LL, RL, LR [see M87* Paper VII], commonly collected into a coherence matrix,

$$\boldsymbol{V}_{ij} = \begin{pmatrix} RR_{ij} & RL_{ij} \\ LR_{ij} & LL_{ij} \end{pmatrix}, \tag{2.5}$$

where the indicies ij refer to the two stations defining a particular baseline. All baselines relevant for EHT are generated at the same time. However, the observed $\boldsymbol{V}_{ij}$ are degraded by aforementioned station gains and polarimetric leakages (D-terms), which means the true coherence matrix are modified as

$$\boldsymbol{V}_{ij} = \boldsymbol{G}_i \boldsymbol{D}_i \bar{\boldsymbol{V}}_{ij} \boldsymbol{D}_j^\dagger \boldsymbol{G}_j^\dagger, \tag{2.6}$$

where $\boldsymbol{G}$ and $\boldsymbol{D}$ contain the gain terms and leakage terms for each station respectively, and $\dagger$ is the complex conjugate transpose. Polarimetric imaging requires full reconstructions

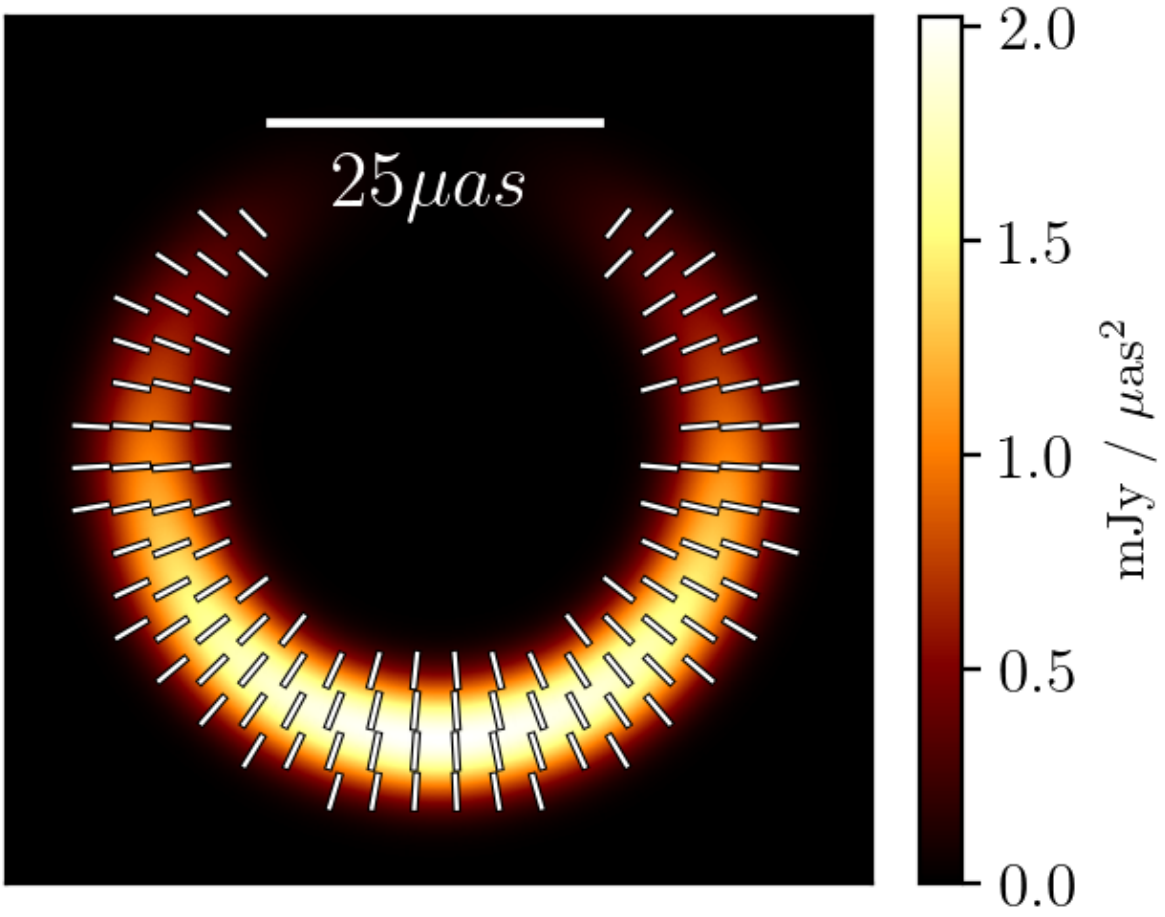

Figure 2.2: The fundamental radial EVPA plot I start from, before adding the additional time-dependent EVPA position angle θ.

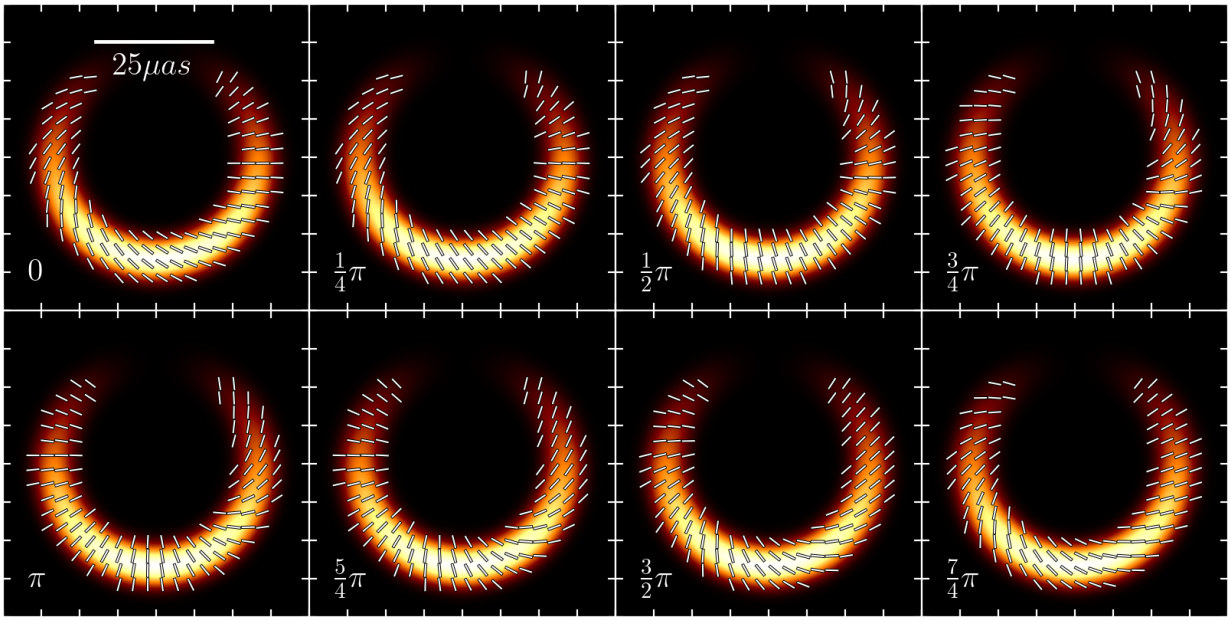

Figure 2.3: Eight frames between 0 and 2π captured from the EVPA time evolution movie of Apr 11, 2017.

of the time-dependent station characteristics (i.e., the $\boldsymbol{G}$ and $\boldsymbol{D}$). However, the immunity/insensitivity of the CT and CCTP to $\boldsymbol{G}$ and $\boldsymbol{D}$ present an opportunity to avoid this process.

The CTs are generated from combinations of $\boldsymbol{V}_{ij}$ on quadrangles, sets of four stations whose baselines form a closed circuit [Broderick and Pesce, 2020].

$$\mathcal{T}_{ijkl} = \frac{1}{2}\mathrm{Tr}\left(\boldsymbol{V}_{ij}\boldsymbol{V}_{kj}^{-1}\boldsymbol{V}_{kl}\boldsymbol{V}_{li}^{-1}\right). \tag{2.7}$$

These are invariant to all linear, station-based corruptions of the coherence matrices, including atmospheric phase delays, receiver gains, and polarization leakage. The full complement of $\mathcal{T}_{ijkl}$ contain all of the residual information in the coherence matrices apart from the standard calibration quantities, and are a superset of the more familiar closure phases and closure amplitudes [Thompson et al., 2017].

While the $\mathcal{T}_{ijkl}$ are generally sensitive to polarized and unpolarized image substructure, a specific combination of them, the CCTP defined by

$$\mathcal{C}_{ijkl} = \mathcal{T}_{ijkl}\mathcal{T}_{ilkj}, \tag{2.8}$$

Parameter	Symbol	2017 Apr 5-6 Fiducial	2017 Apr 10-11 Fiducial	Parameter Range of Sensitivity Check[e]
Annulus radius	R	20μas	20μas	-
Annulus width	w	5μas	5μas	-
Stokes I Position Angle[a]	$\Phi_{\rm I}$	0°	0°	-
Polarization fraction	m	25%	20%	-
Polarization Position Angle[a]	$\Phi_{\rm pol}$	340°	330°	-
Mean EVPA pitch angle[b]	θ_0	30°	30°	-
Variable EVPA pitch angle[b]	θ_1	10°	10°	$0 \sim 20^\circ$
Number of cycles[c]	$n_{\rm cyc}$	0.183	0.183	0.183$\sim$270.29
Axion phase offset[d]	δ	0°	0°	$-90^\circ \sim 90^\circ$

Table 2.1: Geometric Model Parameters and fiducial values for comparison with 2017 EHT observations.
[a]Starting from south, measured east of north.
[b]Measured clockwise relative to radial direction.
[c]Number of full periods in 24 h.
[d]Defined such that $\theta = 0^\circ$ at 0 UT on Apr 5 or on Apr 10, 2017, depending on which dataset I am fitting.
[e]The ranges of parameters used for Figure 2.5, Figure 2.6 and Figure 2.7.

are sensitive only to polarization substructure; in the absence of polarization substructure, the CCTP is identically unity. Therefore, the CCTPs are valuable probes of polarization in much the same way that closure phases are sensitive to asymmetry.

For M87*, the only quadrangle exhibiting CCTPs with the most significant departures from unity, and therefore the most significant evidence for polarized structure, was that combining APEX, ALMA, LMT, and SMT [see Fig 13 of M87* Paper VII]. One potential explanation is that ALMA and LMT have very larger apertures, and are thus the most sensitive stations. Another possible reason is that the ordered polarization pattern indicates that the most power is on scales of a few Gλ, which corresponds to the Chile(ALMA, APEX)-LMT and Chile-SMT baselines (usually below 4 Gλ). Therefore, I construct the CCTPs from the complex visibilities generated by `eht-imaging` on this quadrangle for exploration and comparison with the 2017 EHT data on M87*.

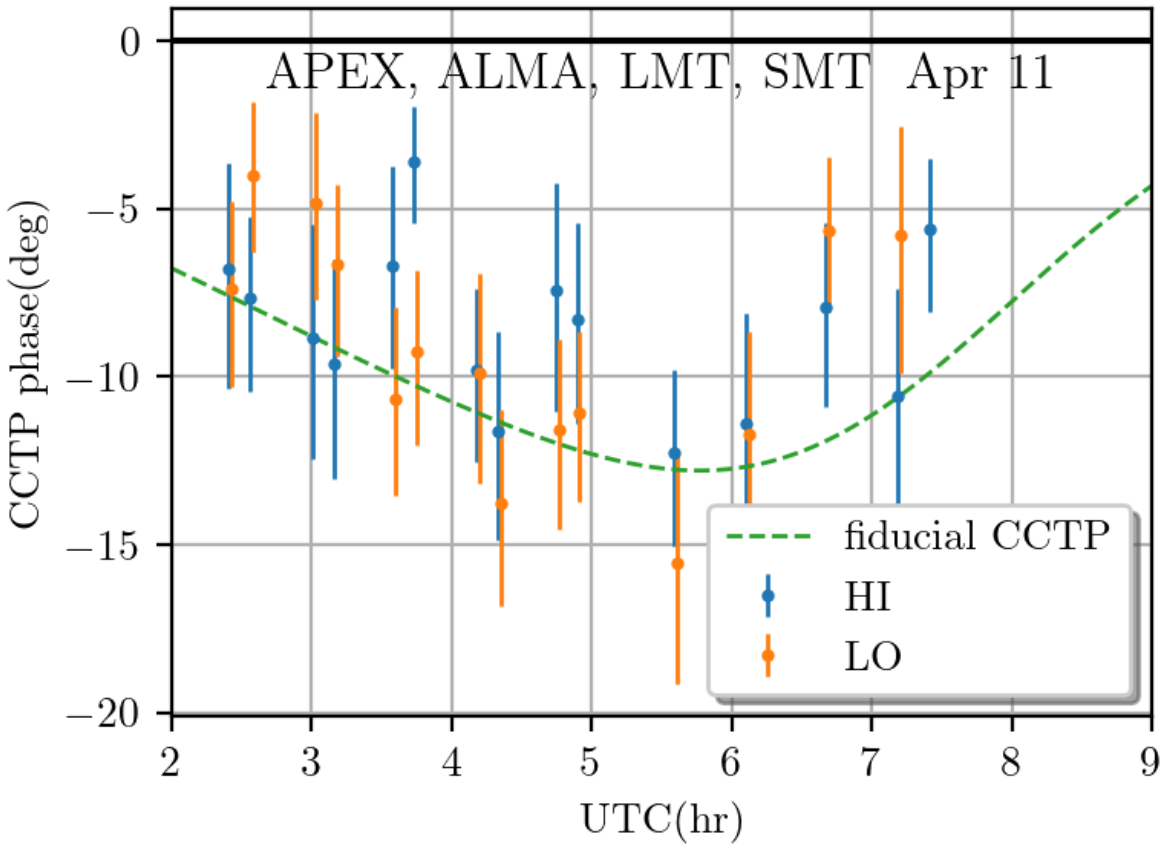

Figure 2.4: HI+LO band CCTP plots for 2017 Apr 11 with overplotted CCTP from the fiducial set of parameters. HI and LO refer to the high frequency band and low frequency band centered at 229.1 GHz and 227.1 GHz, respectively. LO band data are intentionally shifted to the right by 0.02 hrs for better readability. The errorbars in CCTP phases are estimated using Monte Carlo sampling, are purely due to the underlying thermal errors in the visibilities, and are well-approximated as Gaussian errors.

2.3 Sensitivity of CCTPs to Axion Signal

A fiducial set of parameters, listed in Table 2.1, is chosen to qualitatively match the general morphology of the polarized images on 2017 April 11. Figure 2.4 shows the CCTP calculated from the fiducial parameters plotted against read CCTP of 2017 Apr 11. Specifically, I choose the position angle of the maximum brightness in Stokes $\mathcal{I}$ map to lie in the south, the position of the maximum polarized flux to lie in the southwest, and fixed polarization fraction of $m = 25\%$. The fiducial period is selected so that $\alpha \equiv r_g/\lambda_c = 0.4$, consistent with that shown in Figure 1 of Chen et al. [2020], which corresponds to a period of roughly 131 h, or $n_{\rm cyc} = 0.183$ cycles in a 24 h period. The CCTPs produced from this model match those observed on 2017 Apr 11 quantitatively.

Figure 2.5 shows the impact of increasing the variable component of the EVPA pitch angle, θ_1, associated with the axion cloud density. For reference the 2017 Apr 11 high band CCTP measurements are shown in light gray, which indicate that CCTP-based constraints on θ_1 of the order of 10° should be possible. In contrast, variations in θ_0 (not shown) have no impact on the CCTPs; changing θ_0 induces a total rotation in the EVPA across the image to which the closure traces are invariant.

Due to the long fiducial period, modifications of δ can have a large impact on the sensitivity of CCTPs to a putative axion signal. Shown in Figure 2.6 are two models at very different locations in their respective oscillations. The very different sensitivity to θ_1 is easy to understand given the form of θ given in Equation 2.4. Since I am only looking at a fraction of the cycle, when $\delta = 0°$, for small times θ evolves only slowly. However, when $\delta = \pm 90°$, the evolution is maximized. For small times θ depends linearly on time, and thus the variation in the CCTPs is a combination of both θ_1 and the temporal evolution throughout a single night. Unsurprisingly, this behavior is strongly dependent on $n_{\rm cyc}$ as shown in Figure 2.7. Non-zero θ_1 would induce peaks as substructures on the overall CCTP curves, with the number of peaks proportional to $n_{\rm cyc}$. In addition, for shorter periods, or larger $n_{\rm cyc}$, the magnitude of the variation in the CCTPs driven by θ_1 is generally increased, maximizing when $n_{\rm cyc} \gtrsim 1$.

The dependence on δ and $n_{\rm cyc}$ motivates a number of practical concerns for constraining the existence of axion clouds in EHT targets. For M87*, the large SMBH mass requires a large period, and thus small $n_{\rm cyc}$ — constraints will benefit from coherently combining CCTP measurements across many nights. This is further justified by the long intrinsic timescale for astrophysical changes in the emission region.

However, for Sgr A*, the much lower mass requires a smaller axion mass to drive the superradiant instability, and thus shorter orbital period and larger $n_{\rm cyc}$. Simply rescaling

by the SMBH mass, this fiducial M87* model produces $n_{\rm cyc} = 270.29$ for Sgr A*. It is easy to notice the difference in Figure 2.7, from which I conclude that even a single observation night may strongly constrain the existence of an axion cloud in the Galactic center.

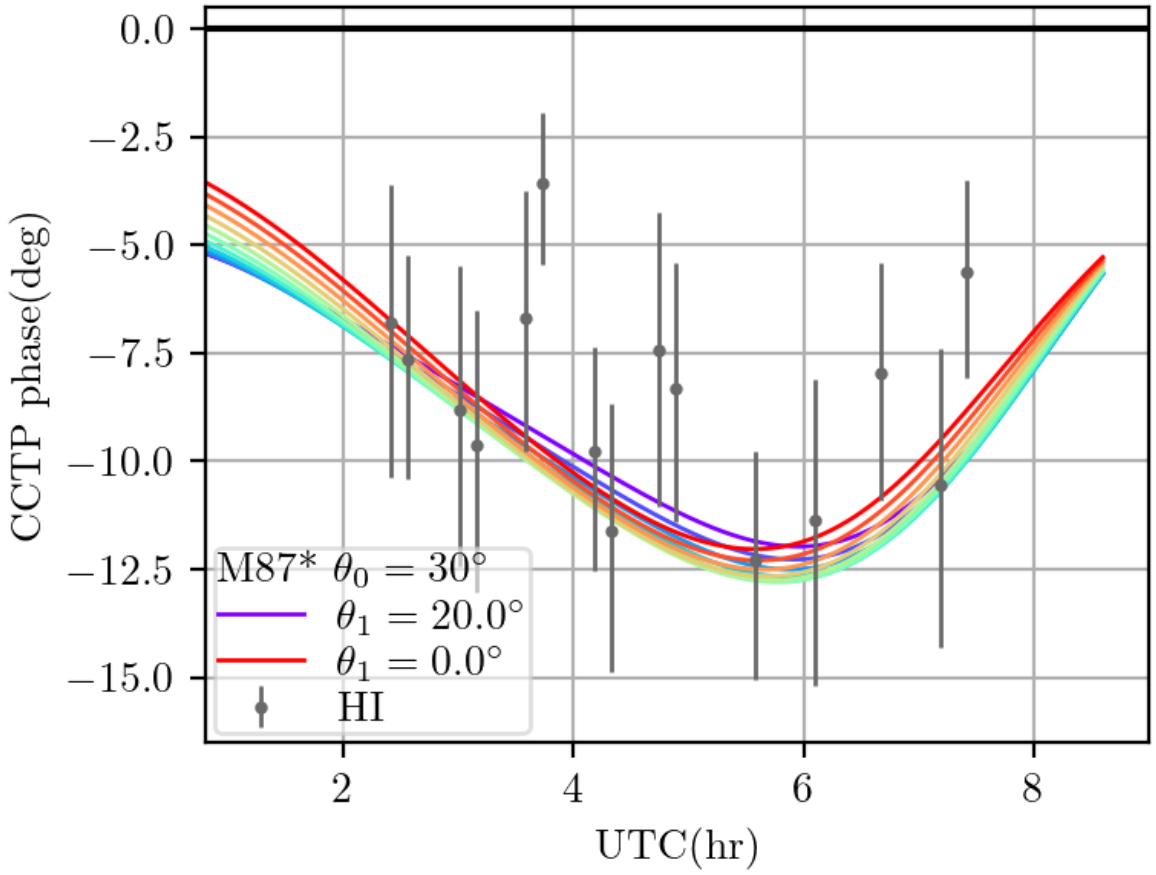

Figure 2.5: Change in θ_1. The first line in the legend indicates the target of the simulated CCTP and the parameter to be varied. From red to purple, the spacing of θ_1 between two consecutive colors is 2°.

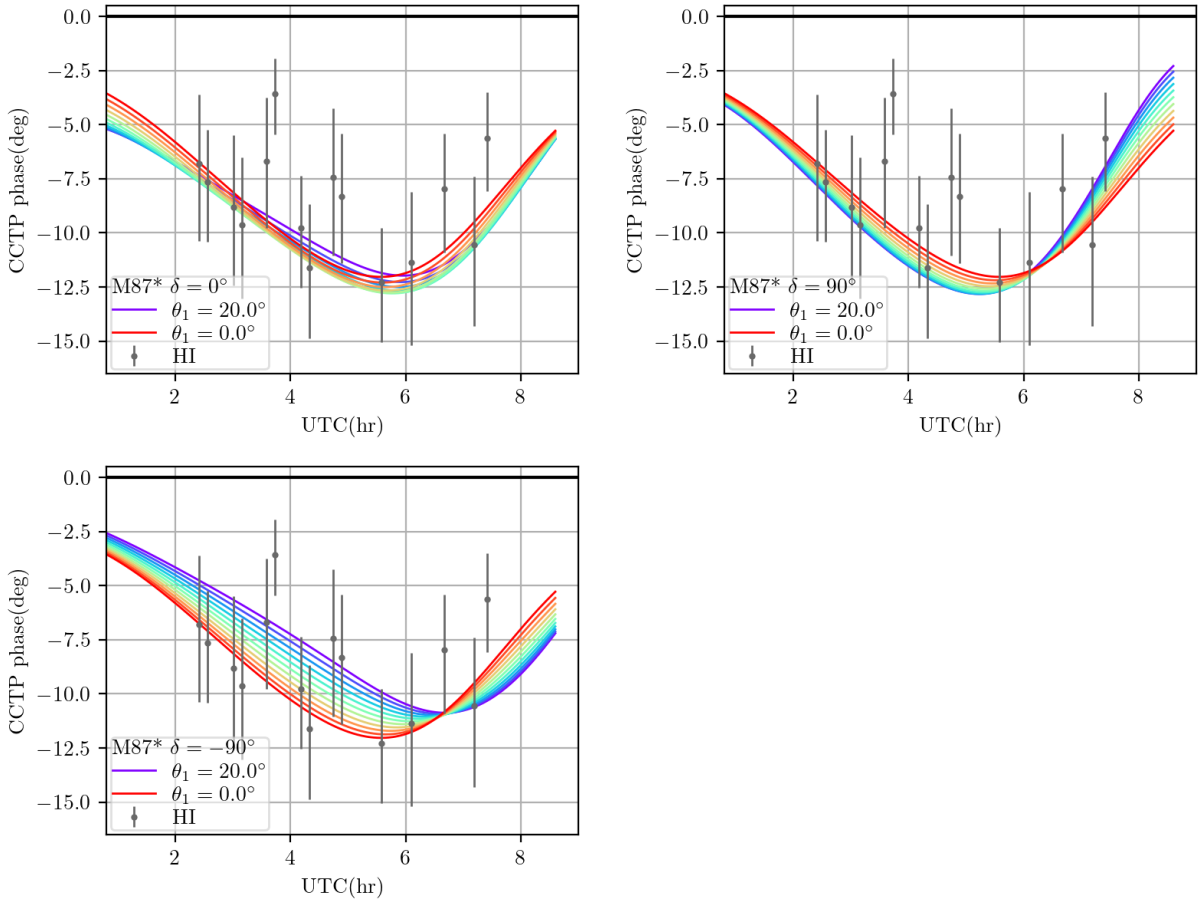

Figure 2.6: Change in δ. The first line in the legend indicates the target of the simulated CCTP and the parameter to be varied. From red to purple, the spacing of θ_1 between two consecutive colors is 2°.

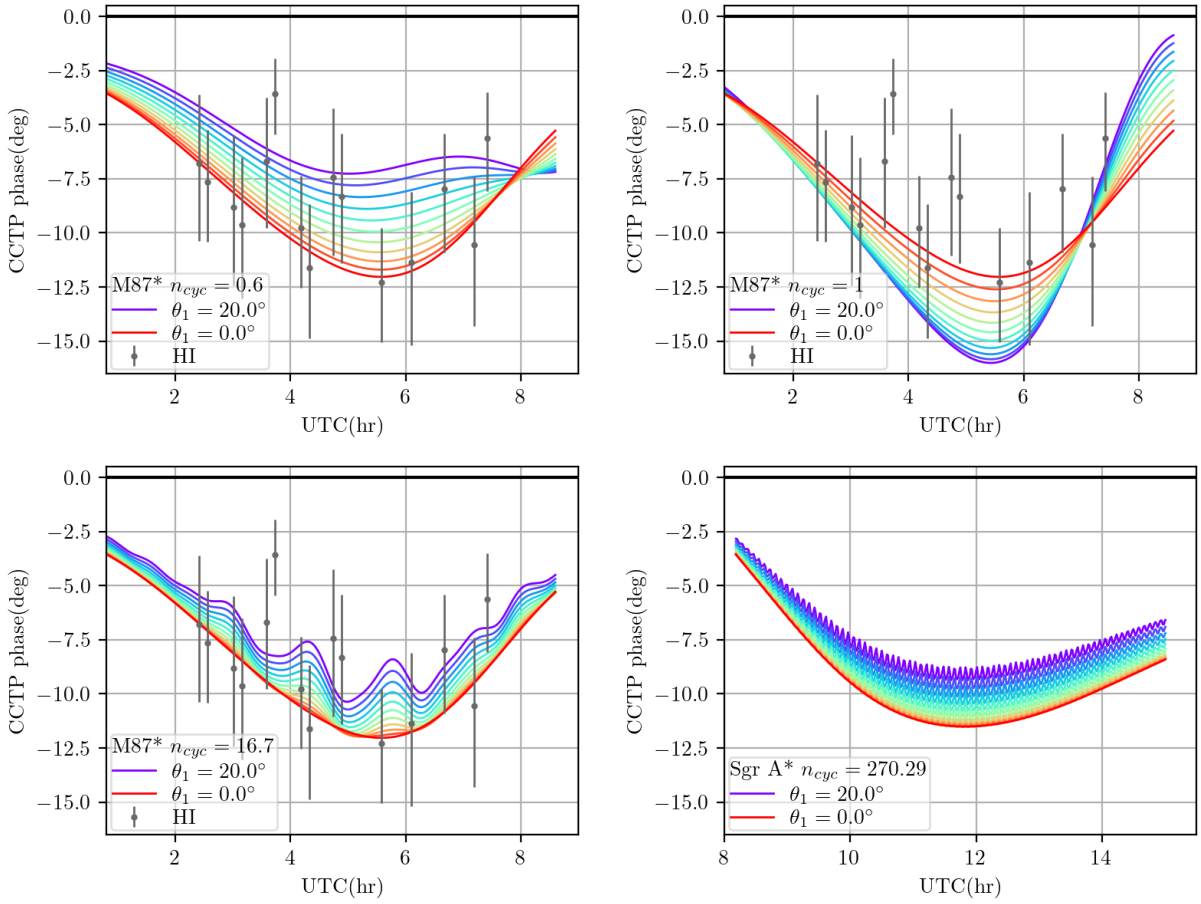

Figure 2.7: Change in n_{cyc}. The first line in the legend indicates the target of the simulated CCTP and the parameter to be varied. From red to purple, the spacing of θ_1 between two consecutive colors is 2°.

Chapter 3

Implications of M87* CCTP Data

Armed with an expectation that CCTPs may be a sensitive discriminator among axion models in M87* and Sgr A*, I perform a number of fits to simulated and real data sets. I begin with a summary of the fitting procedure, followed by demonstration on simulated data sets, and ending with an application to the 2017 EHT M87* data.

3.1 Fit Procedure

In all cases, I make use of the Monte Carlo Markov Chain sampler `emcee` to explore the posterior space of the model parameters [Foreman-Mackey et al., 2013]. To fit the geometric model with the CCTPs of the entire 4 days of observations, Both real and simulated data are grouped into two sets, each contains two consecutive days of observations, i.e Apr 5, 6 and Apr 10, 11, allowing the variability of M87* in a timescale of a week. In addition, a fit directly to Apr 5, 6, 10, 11 is also performed. Beginning with the fiducial model parameters in Table 2.1, I calculate the corresponding CCTP values and then the log-probability by comparing the predicted and observed CCTP values, along with the corresponding errors, and summing over all datapoints, and update them within 200000 samples for a total of 40 walkers in parallel, i.e., a total of 8 million samples. Triangle plots are produced from chains [Foreman-Mackey, 2016], and plots for the joint posterior distributions with axes converted to $\log(c_{a\gamma})$ and α in alignment with Chen et al. [2022b] are generated as the axion limits derived from CCTP analyses. In particular, I transform the θ_1-$n_{\rm cyc}$ plot into the $\log(c_{a\gamma})$-m_a plot with the conversion factors discussed in the appendix.

3.2 Simulated Data Sets

In order to explore the impact of large θ_1 and the significant errorbars that came with the observation data, a total of 4 simulated data sets are created based on the actual mass of M87* and two choices of predetermined θ_1. Posterior distribution plots for the simulated data sets are shown in Figure 3.2.

The null case ($\theta_1 = 0$) shows a clear excluded region of axion parameters in the upper right of the posterior plot, resembling the feature in Figure 4 of Chen et al. [2022b], although my limiy is weaker. However, the case with non-trivial $\theta_1 = 60°$ indicates a significant clump of high probabilities located roughly between $\log(c_{a\gamma}) = 1$ and $\log(c_{a\gamma}) = 2$, where the actual parameters fall in. The "truth" is indeed narrowly constrained. Therefore, I believe the fitting works as expected since I clearly see anticipated behaviors in Figure 3.2, which recovers reasonable values of M87* mass and θ_1, and uncertainties. Overall, considering the fact that simulated data sets were constructing based on the method of control variable, patterns deviating from the null case posterior plot can indicate a possible detection of light axions that can trigger EVPA variations with magnitude above the level which can be explained by the errorbars.

3.3 2017 EHT M87* Campaign

As stated above, fits for EHT data are performed on the 2017 Apr 5, 6 and Apr 10, 11 data sets separately. In addition, a fit to the entire set of data (2017 Apr 5, 6, 10, 11) is also executed. The 2-σ band plots from MCMC fitting for each set are overplotted on real data and shown in Figure 3.1. Posterior distribution plots for the real data sets are shown in Figure 3.3. The posterior plot for Apr 10, 11 clearly matches a non-detection of light axions at even 2-σ and is consistent with the null case posterior plot in Figure 3.2. Although it may seem that on Apr 5, 6, there is a phantom of detection at 2-σ level, the feature of no detection dominates at 3-σ level. Moreover, the fit to the entire data set (lower left of Figure 3.3) preserves the non-detection conclusion. Thus the deviation on Apr 5, 6 is most likely due to fluctuations.

3.4 Discussion

In general, fits for simulated data sets properly recover the undelying predetermined parameters, indicating the feasibility of this method. For EHT 2017 data, at 3-σ level, I

conclude that there is no detection of light axions and arrive at an upper limit. Despite a potential 2-σ suggestion on Apr 5, 6, it is insufficient to make any statement on the existence of light axions.

It is essential to carefully define "detection/non-detection of axions" here. For a non-detection it suffices to conclude that within the current accuracy that the null hypothesis, no axion cloud, is consistent with the observation. Consequently, I exclude parameter spaces above a certain boundary because any light axion with parameters above that boundary will result in an inconsistency with the observed EHT data; conversely, the EVPA variations due to lower density axion clouds are consistent within the formal uncertainties. In order to claim a "detection" of an axion cloud, the elimination of the null hypothesis is necessary but insufficient. In addition, all potential astrophysical origins for the EVPA oscillations must be excluded, and this is something I have yet explored here. Therefore, at present I am only constraining the upper limits of parameters light axions, and the results are consistent with that, as seen in Figure 3.3.

Figure 3.4 summarizes my constraint to light axion parameters derived via the CCTP analysis on the M87* 2017 linear polarization data. The bound on the dimensionless coupling constant becomes weaker for smaller axion masses, primarily due to a smaller value of the radial wave function of the axion cloud and a smaller single-day axion field variation resulting from the longer oscillation period [Chen et al., 2022b]. Despite presenting a modestly weaker limit than the preceding one, this result highlights the feasibility of CCTP analyses for constraining the existence of axion clouds. More importantly, the image-based analysis of Chen et al. [2022b] is inevitably subject to significant underlying systematic uncertainties originating from the estimation of station gains and D-terms, to which the CCTP-based analysis is insensitive. Additionally, the use of CCTP analyses on the polarization data of other SMBHs, for which full polarimetric imaging may be infeasible or impractical, holds potential for cross-validation of the existence of light axions, more is discussed in Chapter 4.

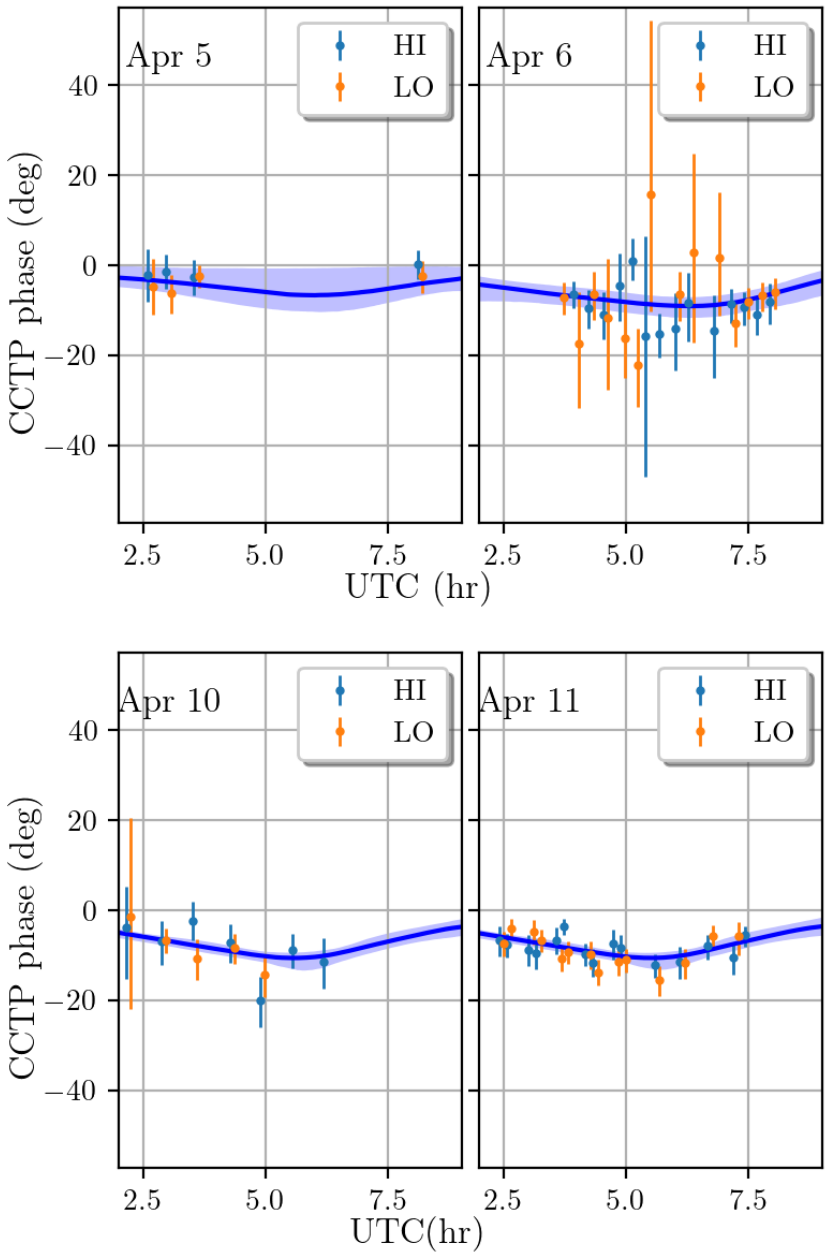

Figure 3.1: 2-σ band plots over the real data, depicted in blue, estimated from the MCMC fitting procedures on all 4 days. The central blue lines indicate the average fitting result.

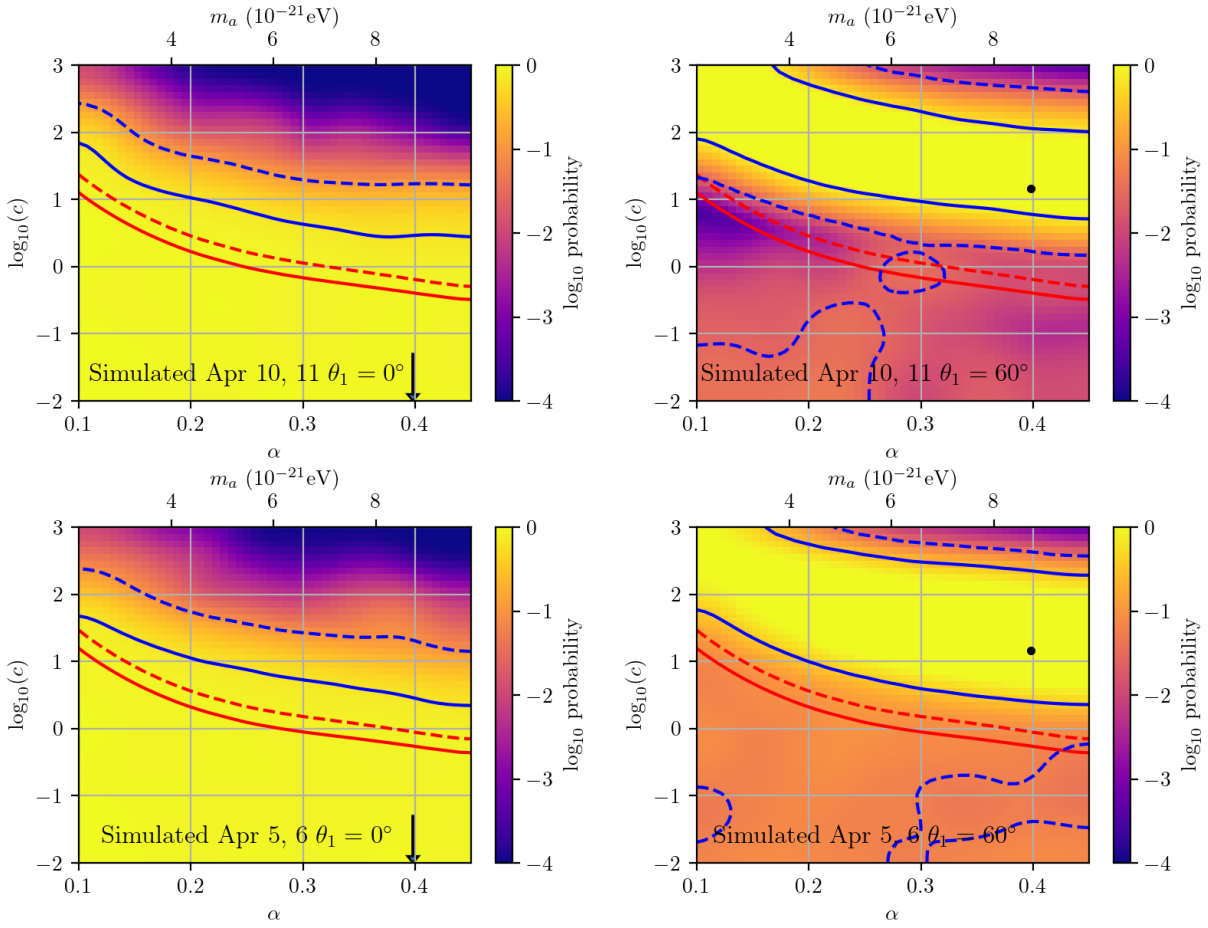

Figure 3.2: Posterior distribution plots for simulated data. Constraints from Chen et al. [2022b] are overplotted as red lines, while the blue lines are my estimates of excluded regions of axion parameters. Dashed lines are 3-σ constraints and solid lines are 2-σ constraints. The negative numbers on the colorbar imply a logscale of the probability in the corresponding posterior plot. The actual parameters used to generate those simulated cases are labeled as black dots on the posterior distribution plots or indicated by black arrows if they fall way below the lower limit.

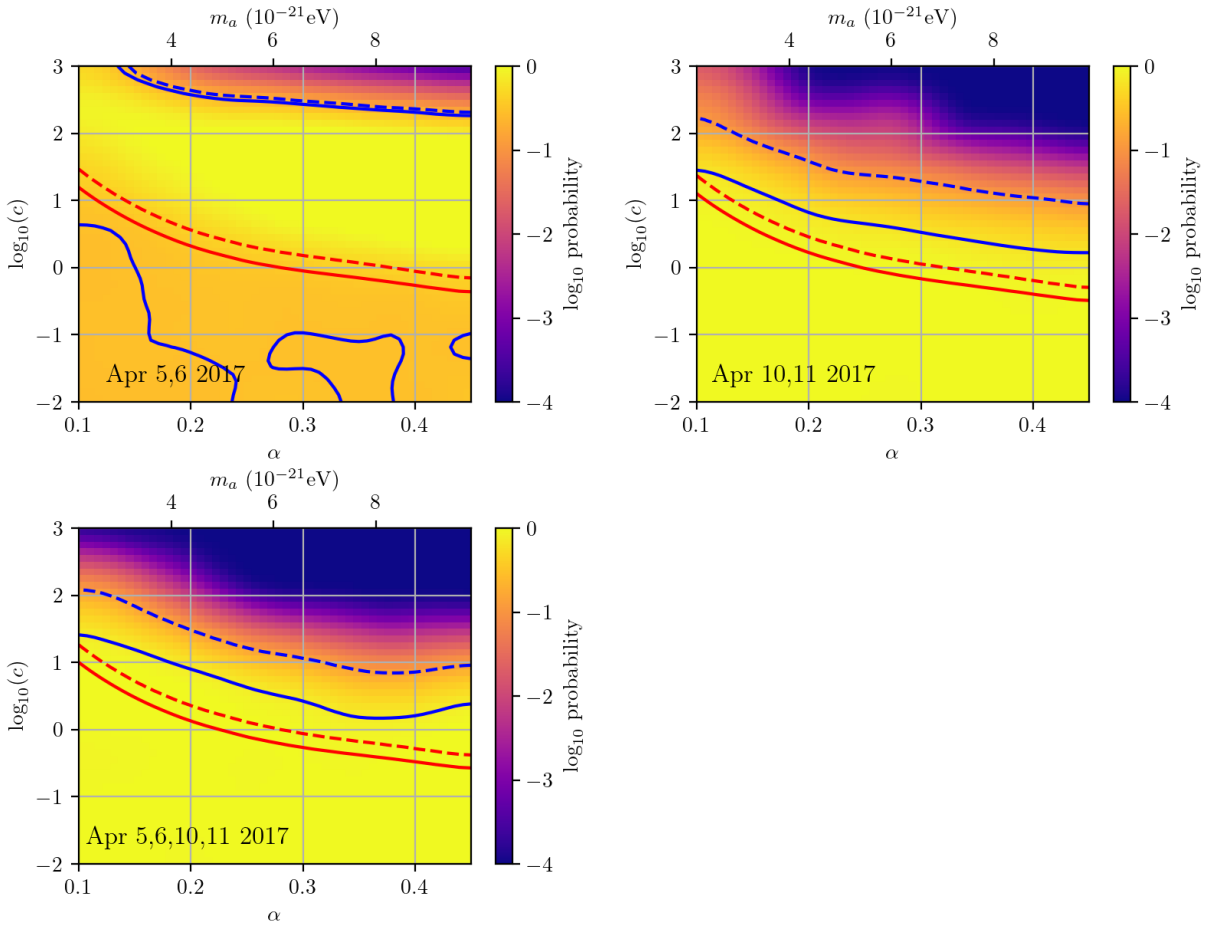

Figure 3.3: Posterior distribution plots for real data. Constraints from Chen et al. [2022b] are overplotted as red lines, while the blue lines are my estimates of excluded regions of axion parameters. Dashed lines are 3-σ constraints and solid lines are 2-σ constraints. The negative numbers on the colorbar imply a logscale of the probability in the corresponding posterior plot.

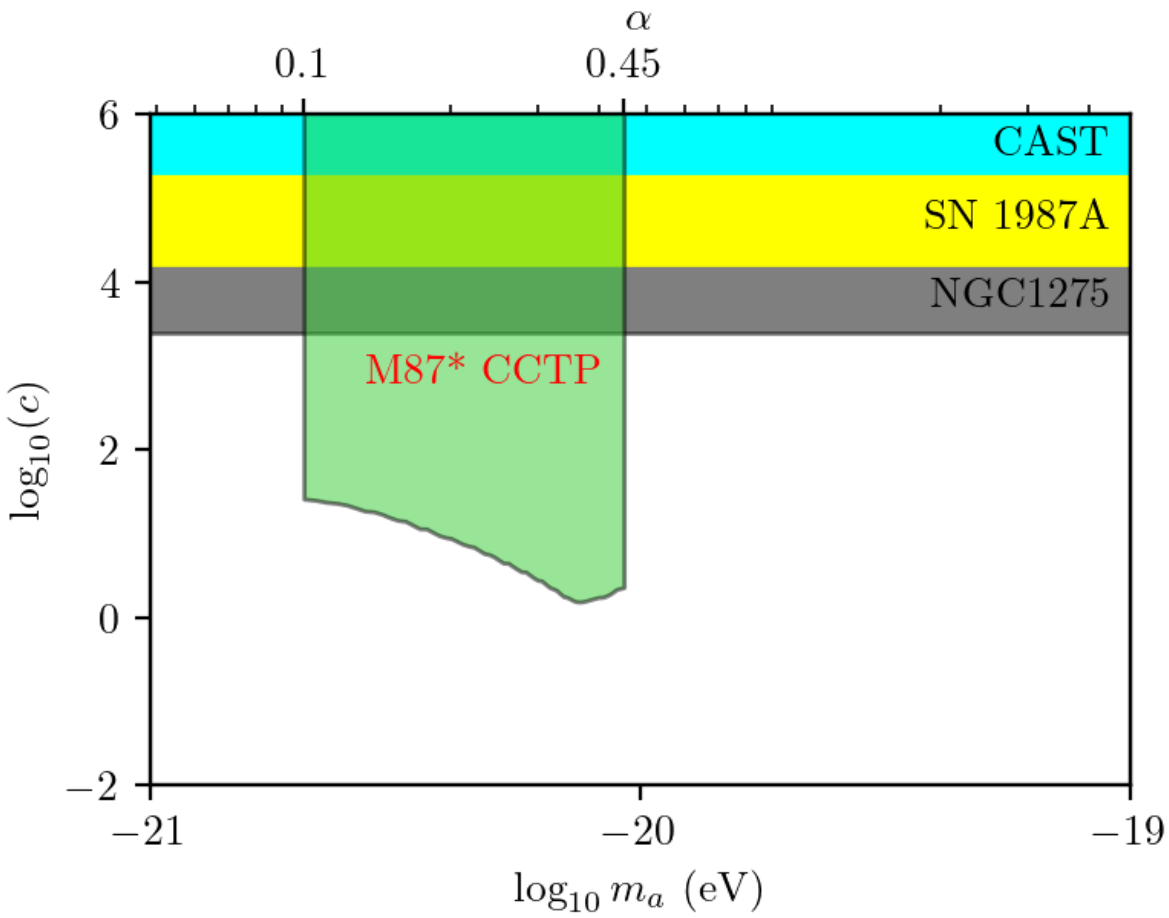

Figure 3.4: The 90% limit on the axion-photon coupling(lime-green), set by the fit to the entire dataset (Apr 5, 6, 10, 11), estimated from the polarimetric data in EHT M87* 2017 campaign via CCTP analysis. In comparison, by assuming $f_a = 10^{15}$GeV, bounds from CAST [Anastassopoulos et al., 2017], SN1987A [Payez et al., 2015] and NGC1275 [Reynolds et al., 2020] are also shown.

Chapter 4

Conclusion and Future Work

4.1 Conclusion

The unprecedented level of sensitivity by EHT through VLBI technique enables in-depth studies of the horizon-scale physics around SMBHs. In this work the polarization signals from a particular SMBH: M87* have been studied with a new, robust tool called CCTP. The unique features of the polarimetric images of M87* provide chances to investigate the mysterious, hypotherical BSM particle: axion (and ALP), and further put constraints on their intrinsic parameters.

I develop a geometric model to describe the time-dependent EVPA oscillation of the EHT images of M87* across the 4 days of observations by extracting the prominent features of a photon ring and the "twisty" linear polarization pattern with azimuthal dependence. This simple model fully captures the characteristics of EVPA variation caused by axion induced birefringence effect. `eht-imaging` processable movies generated from this model are used to produce CCTP curves vs observation time via the novel calibration-insensitive closure trace. Examinations of those curves with different model parameters reveal the significances of impact from axion cloud and the choice of mass of the central SMBH. Fittings to both simulated and real data sets of M87* provide reasonable constraints to light axions, upper-bounded by assuming EVPA oscillation is fully explained by axion-photon coupling.

The final constraint in Figure 3.4 indicates that $\log_{10}(c_{a\gamma})$ is roughly less than 1 for the axion mass m_a in the range from approximately 2.2×10^{-21}eV to 9.9×10^{-21}eV. Previous axion and ALP searches with polarized radio interferometry of nearby SMBHs,

although expanded the parameter space of axion mass and axion-photon coupling constant, inevitably suffers from multiple systematic uncertainties including station gains and polarimetric leakages. On the other hand, the new robust method I presented in this paper used closure trace analyses that can skip through the time-consuming calibration procedures, to constrain light axion and ALP parameters and eventually reached a comparable level to other methods, even with only one set of quadrangle baselines.

4.2 Future Work

As the feasibility of closure trace method being proved, future work should include expanding the number of quadrangles and processing polarization data from other SMBH, especially Sgr A*. More sites began to join the EHT Collaboration in M87* 2018 and later data, expanding the number of available quadrangles significantly. Furthermore, with the improved baseline coverage, spatial and temporal resolution of next-generation EHT in the future [Johnson et al., 2023], a more detailed geometric model can be constructed based on a more precise EVPA movements across multiple days, and an unprecedented level of light axion parameter constraints is promising. This can be seen with a simple, quantitative estimate on the sensitivity improvement. The planned observations with the ngEHT increases from EHT's 4 days to 16 days, and the bandwidth increases from 4 GHz to 64 GHz [Doeleman et al., 2019]. More importantly, the inclusions of 20 stations in ngEHT [Doeleman et al., 2019], compared to 8 stations in EHT 2017 Campaign (which has 19 independent quadrangles), expand the number quadrangles to 341. Therefore it is possible for the ngEHT to improve the precision with which the axion-photon coupling constant, $\log_{10}(c_{a\gamma})$, can be measured by a factor of $\sqrt{4 \times 16 \times 341/19} \sim 34$. Verifying this with simulated data would be a natural future project.

References

C. B. Adams, N. Aggarwal, A. Agrawal, R. Balafendiev, C. Bartram, M. Baryakhtar, H. Bekker, P. Belov, K. K. Berggren, A. Berlin, C. Boutan, D. Bowring, D. Budker, A. Caldwell, and et al. Axion Dark Matter. *arXiv e-prints*, art. arXiv:2203.14923, Mar. 2022. doi: 10.48550/arXiv.2203.14923. URL https://ui.adsabs.harvard.edu/abs/2022arXiv220314923A.

W. Alston, M. Giustini, and P. O. Petrucci. The Super-Massive Black Hole close environment in Active Galactic Nuclei. *arXiv e-prints*, art. arXiv:2206.11790, June 2022. doi: 10.48550/arXiv.2206.11790. URL https://ui.adsabs.harvard.edu/abs/2022arXiv220611790A.

V. Anastassopoulos, S. Aune, K. Barth, A. Belov, H. Bräuninger, G. Cantatore, J. M. Carmona, J. F. Castel, S. A. Cetin, F. Christensen, J. I. Collar, T. Dafni, and et al. New CAST limit on the axion-photon interaction. *Nature Physics*, 13(6):584–590, June 2017. doi: 10.1038/nphys4109. URL https://ui.adsabs.harvard.edu/abs/2017NatPh..13..584A.

A. Arvanitaki and S. Dubovsky. Exploring the string axiverse with precision black hole physics. *PhRvD*, 83(4):044026, Feb. 2011. doi: 10.1103/PhysRevD.83.044026. URL https://ui.adsabs.harvard.edu/abs/2011PhRvD..83d4026A.

A. Arvanitaki, M. Baryakhtar, and X. Huang. Discovering the QCD axion with black holes and gravitational waves. *PhRvD*, 91(8):084011, Apr. 2015. doi: 10.1103/PhysRevD.91.084011. URL https://ui.adsabs.harvard.edu/abs/2015PhRvD..91h4011A.

X. Barcons. Uncovering AGN with X-ray observations. In I. Márquez, J. Masegosa, A. del Olmo, L. Lara, E. García, and J. Molina, editors, *QSO Hosts and Their Environments*, page 357, Jan. 2001. URL https://ui.adsabs.harvard.edu/abs/2001qhte.conf..357B.

B. Boccardi, T. P. Krichbaum, E. Ros, and J. A. Zensus. Radio observations of active galactic nuclei with mm-VLBI. *A&A Rv*, 25(1):4, Nov. 2017. doi: 10.1007/s00159-017-0105-6. URL https://ui.adsabs.harvard.edu/abs/2017A&ARv..25....4B.

A. E. Broderick and D. W. Pesce. Closure Traces: Novel Calibration-insensitive Quantities for Radio Astronomy. *ApJ*, 904(2):126, Dec. 2020. doi: 10.3847/1538-4357/abbd9d. URL https://ui.adsabs.harvard.edu/abs/2020ApJ...904..126B.

S. M. Carroll and G. B. Field. Einstein equivalence principle and the polarization of radio galaxies. *PhRvD*, 43:3789–3793, Jun 1991. doi: 10.1103/PhysRevD.43.3789. URL https://link.aps.org/doi/10.1103/PhysRevD.43.3789.

S. M. Carroll, G. B. Field, and R. Jackiw. Limits on a lorentz- and parity-violating modification of electrodynamics. *PhRvD*, 41:1231–1240, Feb 1990. doi: 10.1103/PhysRevD.41.1231. URL https://link.aps.org/doi/10.1103/PhysRevD.41.1231.

A. A. Chael, M. D. Johnson, K. L. Bouman, L. L. Blackburn, K. Akiyama, and R. Narayan. Interferometric Imaging Directly with Closure Phases and Closure Amplitudes. *ApJ*, 857 (1):23, Apr. 2018. doi: 10.3847/1538-4357/aab6a8. URL https://ui.adsabs.harvard.edu/abs/2018ApJ...857...23C.

Y. Chen, J. Shu, X. Xue, Q. Yuan, and Y. Zhao. Probing Axions with Event Horizon Telescope Polarimetric Measurements. *PhRvL*, 124(6):061102, Feb. 2020. doi: 10.1103/PhysRevLett.124.061102. URL https://ui.adsabs.harvard.edu/abs/2020PhRvL.124f1102C.

Y. Chen, C. Li, Y. Mizuno, J. Shu, X. Xue, Q. Yuan, Y. Zhao, and Z. Zhou. Birefringence tomography for axion cloud. *JCAP*, 2022(9):073, Sept. 2022a. doi: 10.1088/1475-7516/2022/09/073. URL https://ui.adsabs.harvard.edu/abs/2022JCAP...09..073C.

Y. Chen, Y. Liu, R.-S. Lu, Y. Mizuno, J. Shu, X. Xue, Q. Yuan, and Y. Zhao. Stringent axion constraints with Event Horizon Telescope polarimetric measurements of M87⋆. *Nature Astronomy*, 6:592–598, Mar. 2022b. doi: 10.1038/s41550-022-01620-3. URL https://ui.adsabs.harvard.edu/abs/2022NatAs...6..592C.

B. Czerny and K. Hryniewicz. The origin of the broad line region in active galactic nuclei. *A&A*, 525:L8, Jan. 2011. doi: 10.1051/0004-6361/201016025. URL https://ui.adsabs.harvard.edu/abs/2011A&A...525L...8C.

S. Doeleman, L. Blackburn, J. Dexter, J. L. Gomez, M. D. Johnson, D. C. Palumbo, J. Weintroub, J. R. Farah, V. Fish, L. Loinard, C. Lonsdale, G. Narayanan, , and et al.

Studying Black Holes on Horizon Scales with VLBI Ground Arrays. In *Bulletin of the American Astronomical Society*, volume 51, page 256, Sept. 2019. doi: 10.48550/arXiv.1909.01411. URL https://ui.adsabs.harvard.edu/abs/2019BAAS...51g.256D.

S. R. Dolan. Instability of the massive Klein-Gordon field on the Kerr spacetime. *PhRvD*, 76(8):084001, Oct. 2007. doi: 10.1103/PhysRevD.76.084001. URL https://ui.adsabs.harvard.edu/abs/2007PhRvD..76h4001D.

Event Horizon Telescope Collaboration, K. Akiyama, A. Alberdi, W. Alef, K. Asada, R. Azulay, A.-K. Baczko, D. Ball, M. Baloković, J. Barrett, and et al. First M87 Event Horizon Telescope Results. I. The Shadow of the Supermassive Black Hole. *ApJL*, 875:L1, Apr. 2019a. doi: 10.3847/2041-8213/ab0ec7. URL http://adsabs.harvard.edu/abs/2019ApJ...875L...1E.

Event Horizon Telescope Collaboration, K. Akiyama, A. Alberdi, W. Alef, K. Asada, R. Azulay, A.-K. Baczko, D. Ball, M. Baloković, J. Barrett, and et al. First M87 Event Horizon Telescope Results. II. Array and Instrumentation. *ApJL*, 875:L2, Apr. 2019b. doi: 10.3847/2041-8213/ab0c96. URL http://adsabs.harvard.edu/abs/2019ApJ...875L...2E.

Event Horizon Telescope Collaboration, K. Akiyama, A. Alberdi, W. Alef, K. Asada, R. Azulay, A.-K. Baczko, D. Ball, M. Baloković, J. Barrett, and et al. First M87 Event Horizon Telescope Results. III. Data Processing and Calibration. *ApJL*, 875:L3, Apr. 2019c. doi: 10.3847/2041-8213/ab0c57. URL http://adsabs.harvard.edu/abs/2019ApJ...875L...3E.

Event Horizon Telescope Collaboration, K. Akiyama, A. Alberdi, W. Alef, K. Asada, R. Azulay, A.-K. Baczko, D. Ball, M. Baloković, J. Barrett, and et al. First M87 Event Horizon Telescope Results. IV. Imaging the Central Supermassive Black Hole. *ApJL*, 875:L4, Apr. 2019d. doi: 10.3847/2041-8213/ab0e85. URL http://adsabs.harvard.edu/abs/2019ApJ...875L...4E.

Event Horizon Telescope Collaboration, K. Akiyama, A. Alberdi, W. Alef, K. Asada, R. Azulay, A.-K. Baczko, D. Ball, M. Baloković, J. Barrett, and et al. First M87 Event Horizon Telescope Results. V. Physical Origin of the Asymmetric Ring. *ApJL*, 875:L5, Apr. 2019e. doi: 10.3847/2041-8213/ab0f43. URL http://adsabs.harvard.edu/abs/2019ApJ...875L...5E.

Event Horizon Telescope Collaboration, K. Akiyama, A. Alberdi, W. Alef, K. Asada, R. Azulay, A.-K. Baczko, D. Ball, M. Baloković, J. Barrett, and et al. First M87 Event

Horizon Telescope Results. VI. The Shadow and Mass of the Central Black Hole. *ApJL*, 875:L6, Apr. 2019f. doi: 10.3847/2041-8213/ab1141. URL http://adsabs.harvard.edu/abs/2019ApJ...875L...6E.

Event Horizon Telescope Collaboration, K. Akiyama, A. Alberdi, W. Alef, K. Asada, R. Azulay, A.-K. Baczko, D. Ball, M. Baloković, J. Barrett, and et al. First M87 Event Horizon Telescope Results. VII. Polarization of the Ring. *ApJL*, 910(1):L12, Mar. 2021a. doi: 10.3847/2041-8213/abe71d. URL https://ui.adsabs.harvard.edu/abs/2021ApJ...910L..12E.

Event Horizon Telescope Collaboration, K. Akiyama, A. Alberdi, W. Alef, K. Asada, R. Azulay, A.-K. Baczko, D. Ball, M. Baloković, J. Barrett, and et al. First M87 Event Horizon Telescope Results. VIII. Magnetic Field Structure near The Event Horizon. *ApJL*, 910(1):L13, Mar. 2021b. doi: 10.3847/2041-8213/abe4de. URL https://ui.adsabs.harvard.edu/abs/2021ApJ...910L..13E.

D. Foreman-Mackey. corner.py: Scatterplot matrices in python. *The Journal of Open Source Software*, 1(2):24, jun 2016. doi: 10.21105/joss.00024. URL https://doi.org/10.21105/joss.00024.

D. Foreman-Mackey, D. W. Hogg, D. Lang, and J. Goodman. emcee: The MCMC Hammer. *PASP*, 125(925):306, Mar. 2013. doi: 10.1086/670067. URL https://ui.adsabs.harvard.edu/abs/2013PASP..125..306F.

C. M. Gaskell. What broad emission lines tell us about how active galactic nuclei work. *NewAR*, 53(7-10):140–148, July 2009. doi: 10.1016/j.newar.2009.09.006. URL https://ui.adsabs.harvard.edu/abs/2009NewAR..53..140G.

K. Hada, A. Doi, K. Wajima, F. D'Ammando, M. Orienti, M. Giroletti, G. Giovannini, M. Nakamura, and K. Asada. Collimation, Acceleration, and Recollimation Shock in the Jet of Gamma-Ray Emitting Radio-loud Narrow-line Seyfert 1 Galaxy 1H0323+342. *ApJ*, 860(2):141, June 2018. doi: 10.3847/1538-4357/aac49f. URL https://ui.adsabs.harvard.edu/abs/2018ApJ...860..141H.

D. Harari and P. Sikivie. Effects of a Nambu-Goldstone boson on the polarization of radio galaxies and the cosmic microwave background. *PhRvB*, 289(1-2):67–72, Sept. 1992. doi: 10.1016/0370-2693(92)91363-E. URL https://ui.adsabs.harvard.edu/abs/1992PhLB..289...67H.

T. M. Heckman, G. K. Miley, W. J. M. van Breugel, and H. R. Butcher. Emission-line profiles and kinematics of the narrow-line region in Seyfert and radio galaxies. *ApJ*, 247:

403–418, July 1981. doi: 10.1086/159050. URL https://ui.adsabs.harvard.edu/abs/1981ApJ...247..403H.

A. Hook. TASI Lectures on the Strong CP Problem and Axions. In *TASI 2018 - Theory in an Era of Data*, page 4, June 2018. doi: 10.22323/1.333.0004. URL https://ui.adsabs.harvard.edu/abs/2018tasi.confE...4H.

R. C. Jennison. A phase sensitive interferometer technique for the measurement of the Fourier transforms of spatial brightness distributions of small angular extent. *MNRAS*, 118:276, Jan. 1958. doi: 10.1093/mnras/118.3.276. URL https://ui.adsabs.harvard.edu/abs/1958MNRAS.118..276J.

M. D. Johnson, V. L. Fish, S. S. Doeleman, D. P. Marrone, R. L. Plambeck, J. F. C. Wardle, K. Akiyama, K. Asada, C. Beaudoin, L. Blackburn, R. Blundell, G. C. Bower, C. Brinkerink, A. E. Broderick, R. Cappallo, and et al. Resolved magnetic-field structure and variability near the event horizon of Sagittarius A*. *Science*, 350(6265):1242–1245, Dec. 2015. doi: 10.1126/science.aac7087. URL https://ui.adsabs.harvard.edu/abs/2015Sci...350.1242J.

M. D. Johnson, K. Akiyama, L. Blackburn, K. L. Bouman, A. E. Broderick, V. Cardoso, and et al. Key Science Goals for the Next-Generation Event Horizon Telescope. *Galaxies*, 11(3):61, Apr. 2023. doi: 10.3390/galaxies11030061. URL https://ui.adsabs.harvard.edu/abs/2023Galax..11...61J.

A. J. Millar, S. Baum, M. Lawson, and M. C. D. Marsh. Axion-photon conversion in strongly magnetised plasmas. *JCAP*, 2021(11):013, Nov. 2021. doi: 10.1088/1475-7516/2021/11/013. URL https://ui.adsabs.harvard.edu/abs/2021JCAP...11..013M.

A. Mirizzi, G. G. Raffelt1, and P. D. Serpico. Photon-Axion Conversion in Intergalactic Magnetic Fields and Cosmological Consequences. In M. Kuster, G. Raffelt, and B. Beltrán, editors, *Axions*, volume 741, page 115. 2008. doi: 10.1007/978-3-540-73518-2_7. URL https://ui.adsabs.harvard.edu/abs/2008LNP...741..115M.

C. O'Hare. cajohare/axionlimits: Axionlimits. https://cajohare.github.io/AxionLimits/, July 2020.

P. Padovani. Active Galactic Nuclei at all wavelengths and from all angles. *Frontiers in Astronomy and Space Sciences*, 4:35, Nov. 2017. doi: 10.3389/fspas.2017.00035. URL https://ui.adsabs.harvard.edu/abs/2017FrASS...4...35P.

A. Payez, C. Evoli, T. Fischer, M. Giannotti, A. Mirizzi, and A. Ringwald. Revisiting the SN1987A gamma-ray limit on ultralight axion-like particles. *JCAP*, 2015(2):006–006, Feb. 2015. doi: 10.1088/1475-7516/2015/02/006. URL https://ui.adsabs.harvard.edu/abs/2015JCAP...02..006P.

R. D. Peccei and H. R. Quinn. CP conservation in the presence of pseudoparticles. *PhRvL*, 38:1440–1443, Jun 1977. doi: 10.1103/PhysRevLett.38.1440. URL https://link.aps.org/doi/10.1103/PhysRevLett.38.1440.

B. M. Peterson. *An Introduction to Active Galactic Nuclei*. 1997. URL https://ui.adsabs.harvard.edu/abs/1997iagn.book.....P.

A. D. Plascencia and A. Urbano. Black hole superradiance and polarization-dependent bending of light. *JCAP*, 2018(4):059, Apr. 2018. doi: 10.1088/1475-7516/2018/04/059. URL https://ui.adsabs.harvard.edu/abs/2018JCAP...04..059P.

J. Preskill, M. B. Wise, and F. Wilczek. Cosmology of the invisible axion. *PhRvB*, 120(1-3):127–132, Jan. 1983. doi: 10.1016/0370-2693(83)90637-8. URL https://ui.adsabs.harvard.edu/abs/1983PhLB..120..127P.

A. C. S. Readhead, R. C. Walker, T. J. Pearson, and M. H. Cohen. Mapping radio sources with uncalibrated visibility data. *Nature*, 285(5761):137–140, May 1980. doi: 10.1038/285137a0. URL https://ui.adsabs.harvard.edu/abs/1980Natur.285..137R.

C. S. Reynolds, M. C. D. Marsh, H. R. Russell, A. C. Fabian, R. Smith, F. Tombesi, and S. Veilleux. Astrophysical Limits on Very Light Axion-like Particles from Chandra Grating Spectroscopy of NGC 1275. *ApJ*, 890(1):59, Feb. 2020. doi: 10.3847/1538-4357/ab6a0c. URL https://ui.adsabs.harvard.edu/abs/2020ApJ...890...59R.

G. A. Shields. A Brief History of Active Galactic Nuclei. *PASP*, 111(760):661–678, June 1999. doi: 10.1086/316378. URL https://ui.adsabs.harvard.edu/abs/1999PASP..111..661S.

A. R. Thompson, J. M. Moran, and J. Swenson, George W. *Interferometry and Synthesis in Radio Astronomy, 3rd Edition*. 2017. doi: 10.1007/978-3-319-44431-4. URL https://ui.adsabs.harvard.edu/abs/2017isra.book.....T.

R. Q. Twiss, A. W. L. Carter, and A. G. Little. Brightness distribution over some strong radio sources at 1427 Mc/s. *The Observatory*, 80:153–159, Aug. 1960. URL https://ui.adsabs.harvard.edu/abs/1960Obs....80..153T.

Appendix A

Conversion of Factors

The conversion factors between n_{cyc} and the axion mass m_a, and between θ_1 and the coupling constant $c_{a\gamma}$ can be calculated in the following way.

Given that the oscillation frequency of the axion field is $\omega_a \sim m_a$ [Plascencia and Urbano, 2018] and converting everything to SI units, here is the corresponding period

$$\frac{2\pi}{T} = \omega_a = \frac{m_a c^2}{\hbar} \tag{A.1}$$

$$T = \frac{h}{m_a c^2} \tag{A.2}$$

Since n_{cyc} is defined as the number of periods per 24 h, it follows that

$$n_{\mathrm{cyc}} = \frac{24}{T} = \frac{24 m_a c^2}{h} \tag{A.3}$$

However, it is more straightforward to convert n_{cyc} to α in terms of coding and plotting, thus by adopting Equation A.3

$$\alpha = \frac{r_{\mathrm{g}}}{\lambda_c} = \frac{r_{\mathrm{g}} m_a c}{\hbar} \tag{A.4}$$

$$n_{\mathrm{cyc}} = \frac{24c}{2\pi r_{\mathrm{g}}}\alpha \approx 0.458\alpha \tag{A.5}$$

The conversion between θ_1 and $c_{a\gamma}$ rests on the assumption that the amplitude of EVPA variation (θ_1) does not vary much with the azimuthal angle ϕ and is confirmed by Figure 2

of Chen et al. [2022b], therefore I azimuthally average the simulation result of $\mathcal{A}(\phi)/g_{a\gamma}a_{\max}$ in Figure 2 of Chen et al. [2022b] with $H = 0.3$, which parametrizes the thickness of the accretion flow. Therefore,

$$\mathcal{A}'(\phi) \equiv \frac{\mathcal{A}(\phi)}{g_{a\gamma}a_{\max}} \tag{A.6}$$

$$c_{a\gamma} \equiv 2\pi g_{a\gamma} f_a \approx 2\pi g_{a\gamma} a_{\max} \tag{A.7}$$

$$\theta_1 = \langle \mathcal{A}(\phi) \rangle_\phi = \frac{\langle \mathcal{A}'(\phi) \rangle_\phi}{2\pi} c_{a\gamma} \tag{A.8}$$

Note that the curve of $\mathcal{A}'(\phi)$ depends on α, thus Equation A.8 are executed for a list of evenly spaced α from 0.1 to 0.45.